Stem Cell Reports
Article

ISSCR

OPEN ACCESS

Fibronectin Patches as Anchoring Points for Force Sensing and Transmission in Human Induced Pluripotent Stem Cell-Derived Pericytes

Olga Iendaltseva,[1,2] Valeria V. Orlova,[3] Christine L. Mummery,[3] Erik H.J. Danen,[2,4,*] and Thomas Schmidt[1,4,*]
[1]Physics of Life Processes, Leiden Institute of Physics, Leiden University, Einsteinweg 55, Leiden, South Holland 2333 CC, the Netherlands
[2]Division of Drug Discovery and Safety, Leiden Academic Center for Drug Research, Leiden University, Einsteinweg 55, Leiden, South Holland 2333 CC, the Netherlands
[3]Department of Anatomy and Embryology, Leiden University Medical Center (LUMC), Leiden, South Holland, the Netherlands
[4]Co-senior author
*Correspondence: e.danen@lacdr.leidenuniv.nl (E.H.J.D.), schmidt@physics.leidenuniv.nl (T.S.)
https://doi.org/10.1016/j.stemcr.2020.05.001

SUMMARY

Pericytes (PCs) have been reported to contribute to the mechanoregulation of the capillary diameter and blood flow in health and disease. How this is realized remains poorly understood. We designed several models representing basement membrane (BM) in between PCs and endothelial cells (ECs). These models captured a unique protein organization with micron-sized FN patches surrounded by laminin (LM) and allowed to obtain quantitative information on PC morphology and contractility. Using human induced pluripotent stem cell-derived PCs, we could address mechanical aspects of mid-capillary PC behavior *in vitro*. Our results showed that PCs strongly prefer FN patches over LM for adhesion formation, have an optimal stiffness for spreading in the range of EC rigidity, and react in a non-canonical way with increased traction forces and reduced spreading on other stiffness then the optimal. Our approach opens possibilities to further study PC force regulation under well-controlled conditions.

INTRODUCTION

Pericytes (PCs) cover the majority of all capillaries in the human body (Zimmermann, 1923). PCs express markers that are shared with mesenchymal stem cells and smooth muscle cells, but in mid-capillary regions lack smooth muscle actin (SMA) expression (Armulik et al., 2011; Paula et al., 2006). PCs have been shown to promote regulation of vascular development, stabilization and maturation of vessels, and the maintenance of the blood-brain barrier (Armulik et al., 2010; Bell et al., 2010). Although PCs are essential for the development of the vascular tree (Gerhardt et al., 2000), their precise role in the control of blood flow through capillaries is still highly debated (Hill et al., 2015; Mishra et al., 2016). PCs are embedded in the capillary basement membrane (BM) and develop characteristic branched processes around microvessels (Armulik et al., 2011; Zimmermann, 1923). This morphology, together with the presence of contractile proteins, such as actin, high concentration of myosin, tropomyosin (Joyce et al., 1985a, 1985b; Le Beux and Willemot, 1978; Wallow and Burnside, 1980), suggests their functional role in applying mechanical forces to strengthen the blood vessel wall, and their participation in the regulation of microvascular blood flow in particular in the brain (Hamilton et al., 2010; Peppiatt et al., 2006). Notably, dysfunction or loss of PCs has been implicated in pathologies such as cerebral ischemia, Alzheimer disease, and diabetic retinopathy (Hall, 2006; Hall et al., 2014; Kisler et al., 2017; Yemisci et al., 2009). Thus, PC-endothelial cell (EC) mechanical interaction represents a potential target for therapy in such conditions.

PCs and ECs build up a variety of mechanical and biochemical interconnections. They use peg-and-socket contacts that contain gap junctions (Fujimoto, 1995) for direct communication and signaling, cell-to-cell adhesions by N-cadherins (Tillet et al., 2005), and integrin-mediated binding of both cell types to the extracellular matrix of the BM of the capillaries (Stratman et al., 2009). A critical component of the proper PC/EC assembly and vessel formation is EphrinB2 reverse signaling. Initial cell-to-cell contact during angiogenesis leads to EphrinB2 engagement by EphB membrane receptors and subsequent EphrinB2 phosphorylation. EphrinB2 phosphorylation, in turn, starts reverse signaling that promotes cell-to-cell adhesion formation (Noberini et al., 2011; Salvucci et al., 2009). In particular, the integrins and N-cadherins provide two independent adhesion systems that allow PCs to apply forces to their environment, thereby affecting the blood flow in the capillary. It has been shown that PC-EC connections through N-cadherins occur mainly during angiogenesis, being lost with vessel maturation and BM generation (Ferreri et al., 2008; Gerhardt et al., 1999). Hence, in mature resting vasculature the mechanical PC-EC connection is dominated by BM-mediated integrin adhesion. The BM in capillaries contains collagen type IV in the outer layer and laminin (LM)-411/511 in the inner layer close to the ECs (Halfter et al., 2013; Yousif et al., 2013). PCs are situated within the BM where they may bind collagen and LM. Yet, electron microscopical analysis further suggests a role for 0.2–2-μm deposits of fibronectin (FN) as specific anchoring points (Armulik et al., 2005; Courtoy and Boyles, 1983; Winkler et al., 2011) (Figure 1A).

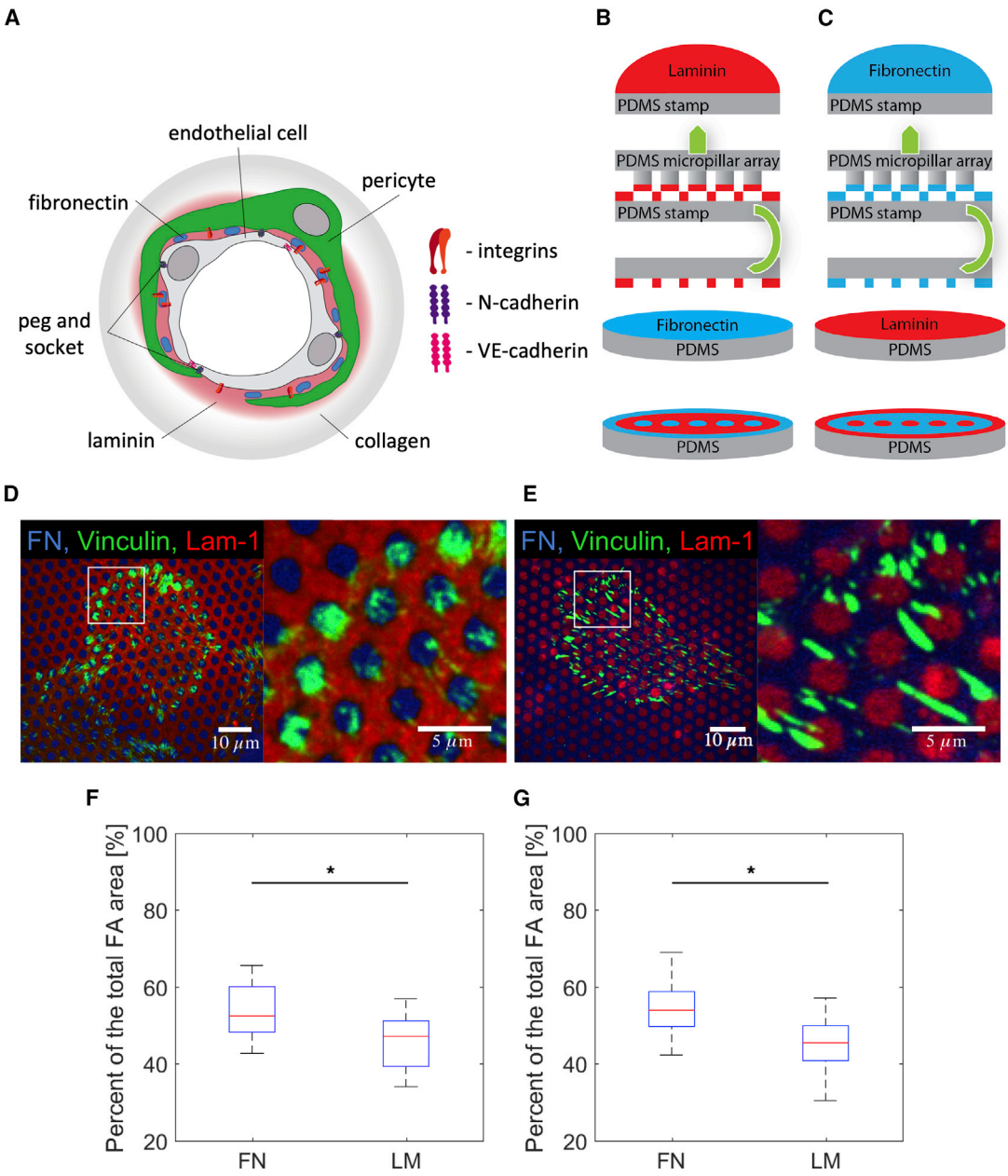

Figure 1. PCs Placed on PDMS Flat Surfaces Stamped with FN and LM-111

(A) Schematic representation of the capillary BM. LM-411/511 and collagen IV are main components that form two layers. FN deposits are embedded into the LM part of the BM and situated in the PC-EC interstitia.

(B and C) (B) Microcontact printing scheme for FN spots surrounded by LM-111 and (C) microcontact printing scheme for LM-111 spots surrounded by FN.

(D) Confocal immunofluorescence images of PCs (dif31) seeded on the type of pattern depicted in (B) with vinculin labeled (green).

(E) Confocal immunofluorescence images of PCs (dif31) seeded on the type of pattern depicted in (C) with vinculin labeled (green).

(F) Percentage of PC (dif31) focal adhesions (FAs) located on FN and LM for (D).

(G) Percentage of PC (dif31) FAs located on FN and LM for (E).

In (F) and (G), the results are derived from three independent experiments performed with a minimum of two replicates. At least ten images were analyzed from each sample. NS, $p > 0.05$, *$p < 0.05$, **$p < 0.005$, ***$p < 0.0005$ according to the Mann-Whitney test. See also Figure S1.

PCs may play an important role in mechanical regulation of the vasculature by providing additional mechanical strength to the endothelium or by regulating blood flow by their contractility. How this is realized is poorly understood, yet understanding of this process might lead to novel concepts in treatment of pathological conditions, and to the identification of novel targets for therapy. Here, we developed an *in vitro* model to investigate mechanical aspects of PC behavior. We utilized our previously described human induced pluripotent stem cell-derived PCs (hiPSCs) with a close to mid-capillary PC phenotype, lacking SMA expression (Orlova et al., 2014a, 2014b). Micropatterned surfaces of LM and FN mimicking BM structures were generated on surfaces varying in mechanical stiffness and in topography. This allowed us to obtain quantitative information on cell morphology and cell contractility. Our results show that (1) PCs strongly prefer FN over LM for adhesion formation, (2) PCs sense a preferred FN substrate stiffness for spreading, and (3) PCs respond to either lower or higher stiffness with increased traction forces, altered cytoskeletal organization, and decreased cell spreading. Our results suggest that FN deposits, as observed in the endothelial BM by electron microscopy, provide the anchoring points for mechanical regulation of capillaries by PCs.

RESULTS

Preferred Binding of PCs to FN Patches on Multilayered Substrates

We investigated whether PCs may preferentially use FN deposits for attachment onto capillaries. As a source for PCs, we used hiPSC line LUMC06iCTRL-derived PCs (Dambrot et al., 2013; Orlova et al., 2014b). As hallmarks for PCs, these cells lacked the endothelial marker CD31, they expressed the PC/mesenchymal stem cell markers PDGFRβ, NG2, CD146, CD44, CD73, and CD105, they expressed very little to no SMA, very little SMC markers, such as (SM)22 and calponin (CNN1), all distinguishing them from SMCs. Moreover, as we described earlier, these PCs promote vascular development in PC-EC co-cultures (Orlova et al., 2014a, 2014b).

We modeled LM and FN arrangements in the endothelium-PC interstitia, which has been described previously by electron microscopy (Courtoy and Boyles, 1983). In electron microscopy studies it was shown that FN was arranged in the form of micrometer-sized patches surrounded by LM-411/511 within the BM of capillaries (Figure 1A). To mimic the *in vivo* observations in our *in vitro* experiments we used a multilayer stamp-off method (Desai et al., 2014) (Figure 1). First, a polydimethylsiloxane (PDMS) micropillar array consisting of 2-μm-wide pillars in a hexagonal arrangement of 2-μm spacing, activated in an UV-Ozone cleaner was pressed onto and released from an LM monolayer deposited on a flat PDMS substrate. The procedure left a homogeneous LM layer with patterned holes on the flat PDMS stamp. Subsequently, this layer was transferred onto a second flat FN-coated PDMS surface. In the resulting multilayered surface, FN was accessible through the holes in the LM layer (Figure 1B). For visualization FN was mixed with a low amount (<1%) of Alexa 405 conjugated FN. LM-111 was visualized using an anti-LM-111 antibody followed by staining with an Alexa 647-coupled secondary antibody.

PCs were incubated for 4 h on the patterned substrates, fixed, and stained for F-actin and cell-matrix adhesion proteins. PCs could readily attach and spread on substrates coated with either LM or FN monolayers. However, in the patterned combined protein model, cells strongly preferred to attach to FN patches and avoided areas covered by LM. Vinculin and α_v-integrin staining showed cell-matrix adhesions formed preferentially on FN patches, avoiding areas containing LM (Figures 1D, 1F, and S1A).

To rule out effects caused by the order in which FN and LM were stamped on the surface, an inverse approach was taken. First the stamp-off method was used to create holes in the FN monolayer, which was subsequently transferred onto a flat PDMS surface coated with LM (Figure 1C). Again, vinculin staining revealed that PCs formed cell-matrix adhesions almost exclusively on the FN-coated area, whereas LM-111-coated areas were avoided (Figures 1E and 1G).

We further generated substrates consisting of crossing stripes of LM and FN by stamping a PDMS surface with a grid of 20- to 60-μm LM-111 and 20-μm FN lines (Figure 2A). Cells aligned on top of the FN lines and avoided areas that were stamped by LM. Vinculin staining showed that PCs developed cell-matrix contacts mainly on the vertical FN stripes, but not with the horizontal LM lines (Figures 2C and 2E). Finally, we combined the two micro-structuring techniques and generated surfaces in which 20-μm FN lines were placed under a layer of LM into which 2-μm-diameter holes were incorporated (Figure 2B). Strikingly, PCs were able to sense the small regions where FN was exposed through the holes in the LM layer, localized adhesions at these spots, and fully aligned to the FN stripes (Figure 2D).

Together, our data showed that PCs adhered preferentially to FN, while avoiding LM areas when FN was present. This suggests that FN deposits in the PC-EC interstitia in capillaries, as previously identified by electron microscopy (Armulik et al., 2005; Courtoy and Boyles, 1983; Winkler et al., 2011), may indeed serve as preferred points for PC attachment to capillaries in the capillary BM.

Highest PC Spreading Is Accompanied by Lowest Force Application on FN Substrates of Intermediate Stiffness

Next, we investigated whether FN deposits serve as mechanical anchoring points where PCs can sense and

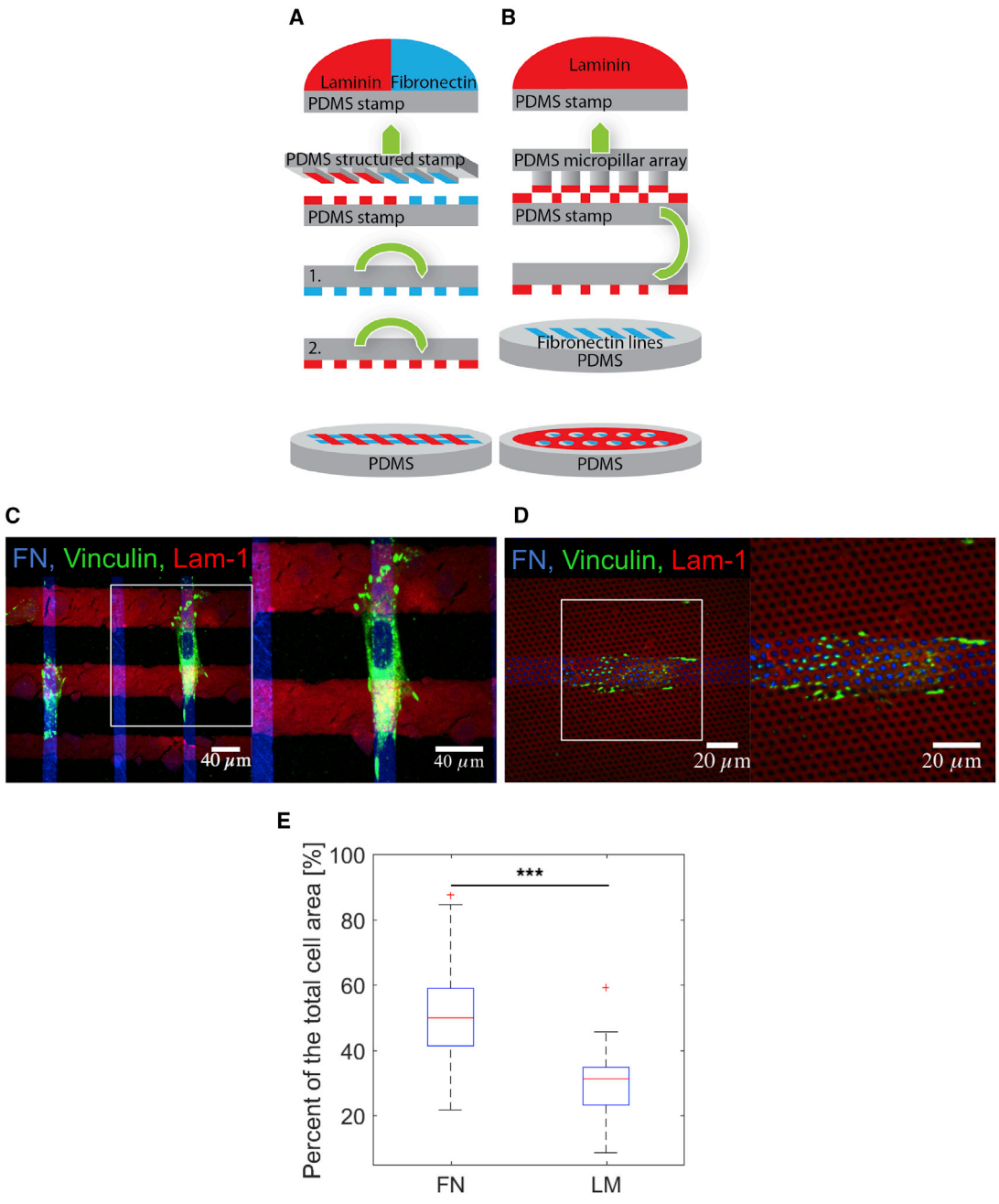

Figure 2. PCs Placed on PDMS Flat Surfaces Stamped with FN and LM-111

(A and B) Microcontact printing schemes for patterns with (A) a grid of crossing LM-111 and FN lines and (B) FN lines stamped under a layer of LM-111 with holes.

(C) Confocal immunofluorescence images of PCs (dif31) seeded on the type of pattern depicted in (A) with vinculin labeled (green).

(D) Confocal immunofluorescence images of PCs (dif31) seeded on the type of pattern depicted in (B) with vinculin labeled (green).

Percentage of PC (dif31) focal adhesions (FAs) located on FN and LM for (E).

In (E), the results are derived from three independent experiments performed with a minimum of two replicates. At least ten images were analyzed from each sample. NS, $p > 0.05$, *$p < 0.05$, **$p < 0.005$, ***$p < 0.0005$ according to the Mann-Whitney test.

respond to variations in mechanical properties of capillaries and, vice versa, apply forces to mechanically modulate the extracellular matrix. As a model, PDMS micropillar arrays were generated using the same geometry as described above (Figure 3A). By varying the height of the pillars between 3 and 7 μm the effective stiffness of the

A

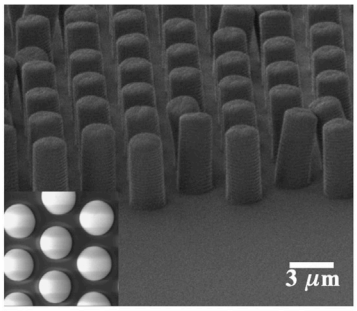

B

Stiffness (kPa)	Height (μm)	Diameter (μm)
11.6	6.9	2
29.5	6.1	2.1
47.2	4.1	1.9
137	3.2	2

C

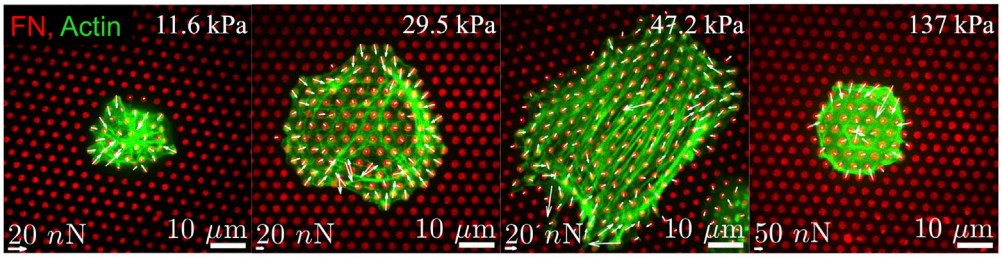

D

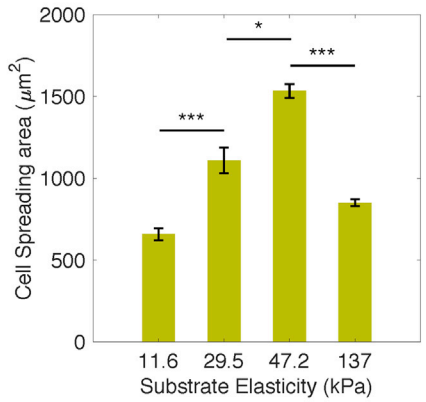

E

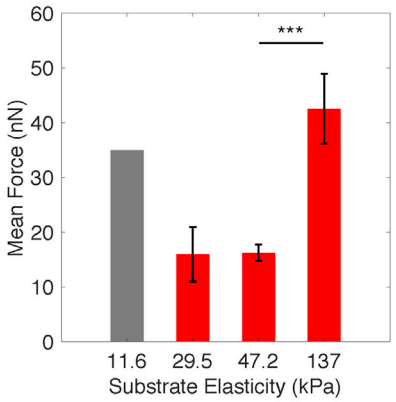

F

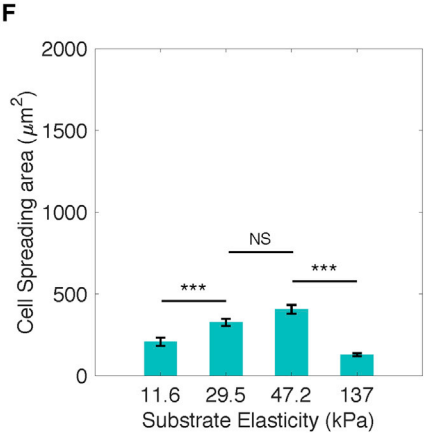

G

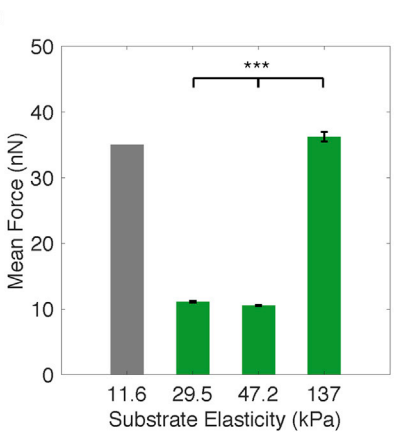

(legend on next page)

arrays was 11.6, 29.5, 47.2, and 137 kPa, respectively (Figure 3B). This range of stiffness resembles that reported for a variety of tissues (Okamoto et al., 2017; Hong et al., 2015). The pillar tops were functionalized with FN to which a low amount (<1%) of Alexa 405/647-labeled FN was added. Such fluorescence labeling allowed monitoring pillar deflections and calculation of cellular traction forces to an accuracy of 0.5 nN using a fluorescence microscope (Figure 3C) (van Hoorn et al., 2014).

PCs derived from two independent differentiations (dif31 and dif43) were seeded onto the pillar arrays, fixed after 4 h, and stained for F-actin. Previously we showed that fixation had negligible effect on the analysis of cell spreading and force measurements (Balcioglu et al., 2015). PC spreading and force exertion varied with variations in substrate stiffness between 12 and 137 kPa. Spreading was highest at an intermediate substrate stiffness between 30 and 47 kPa, resulting in a mean cell area of up to 1,500 μm^2 for one PC (dif31) line, and ~500 μm^2 for another PC (dif43) line. Spreading significantly decreased at both lower and higher substrate stiffness to below 800 μm^2 for PC (dif31) line and ~200 μm^2 for PC (dif43) line (Figures 3D and 3F). The optimal spreading on intermediate substrate stiffness was paralleled by a low cellular force generation of 10–15 nN/pillar for both PC lines (Figures 3E and 3G). On pillars of either lower or higher stiffness, the decrease in spreading was accompanied by significantly higher force generation, reaching 35–40 nN/pillar for both PC lines (note: the high mean force value at the lowest substrate stiffness of 11.6 kPa refers to a lower limit since ~25% of the pillars collapsed onto each other due to excessive forces under these conditions and could not be analyzed).

This behavior was different from the behavior of fibroblasts. For both SV80 (Figures S2A and S2B) and NIH-3T3 (Figures S2C and S2D) cellular forces gradually increased with substrate stiffness, in line with previous reports (Pelham and Wang, 1997; Yeung et al., 2005). Across this stiffness range, spreading was largely constant for both fibroblast lines.

We further analyzed how variations in substrate stiffness affected formation and properties of cell-matrix adhesions. Immunofluorescence staining was applied to detect the focal adhesion proteins vinculin, paxillin, and talin on top of the micropillars. As reported earlier, focal adhesions developed solely on pillars at which cells applied a force (van Hoorn et al., 2014). The average cell-matrix adhesion area was determined (Figure 4). Remarkably, for all components analyzed, the cell-matrix adhesion area decreased from ~2 μm^2 at intermediate stiffness substrates to <1.5 μm^2 at high stiffness substrates (Figure 4G). Surprisingly, the correlations between size of the cell-matrix adhesion, the applied cellular force, and the substrate stiffness, as reported for various fibroblast cell lines (Balaban et al., 2001; Trichet et al., 2012; van Hoorn et al., 2014), did not hold for the hiPSC-derived PCs studied here.

Together, our findings suggest that PCs bind specifically to FN patches, and sense and respond to changes in stiffness between 12 and 137 kPa. In contrast to fibroblasts for which we observed a continued increase in traction force with increasing substrate stiffness, PCs suppress traction forces and increase cell spreading within 30–50 kPa matrix stiffness range, while applying strong traction forces accompanied by limited cell spreading on both soft and stiff substrates.

A Switch in PC Cytoskeletal Organization on Stiff Substrates

To further examine what may underlie the increased force application at reduced focal adhesion area on stiff micropillars, we analyzed the organization of the F-actin cytoskeleton (Figure 5A). F-Actin was labeled by phalloidin. The 3D structure of the actin skeleton was imaged for the various substrate stiffnesses. While straight, elongated F-actin stress fibers were visible on pillars of intermediate stiffness, on stiff micropillars PCs appeared to engulf the pillars and form ring-like F-actin structures that embraced multiple pillars. Notably, all array surfaces, excluding the

Figure 3. PCs Placed on PDMS Micropillar Arrays of Different Stiffness Stamped with FN

(A) An example scanning electron microscope image of the micropillar array.

(B) A table with pillar dimensions per stiffness used for experiments.

(C) Confocal immunofluorescence images showing PCs (dif31) (actin staining in green) seeded on PDMS micropillar arrays of four different stiffness (from left to right: 11.6, 29.5, 47.2, and 137 kPa), functionalized with FN (red). Forces exerted on pillars are depicted with white arrows.

(D and F) Average cell spreading area for two different PC lines, (D) PC dif31 and (F) PC dif43, on PDMS micropillar arrays after 4 h of incubation.

(E and G) Average force application for two different PC lines, (E) PC dif31 and (G) PC dif43, measured after 4 h of incubation on PDMS micropillar arrays. Note that on 11.6-kPa micropillar arrays ~25% pillars collapsed due to the apparent high forces, precluding deflection analysis. The gray bar represents the minimal force necessary for the pillar deflection equal to the interpillar distance. Actual average force may be higher. All error bars are SEM derived from five for PC dif31 line and three for PC dif43 line independent experiments performed in a minimum of two replicates. At least 30 cells were analyzed from each sample.

NS, $p > 0.05$, *$p < 0.05$, **$p < 0.005$, ***$p < 0.0005$ according to the Mann-Whitney test (A, B, and D) or ANOVA (E). See also Figure S2.

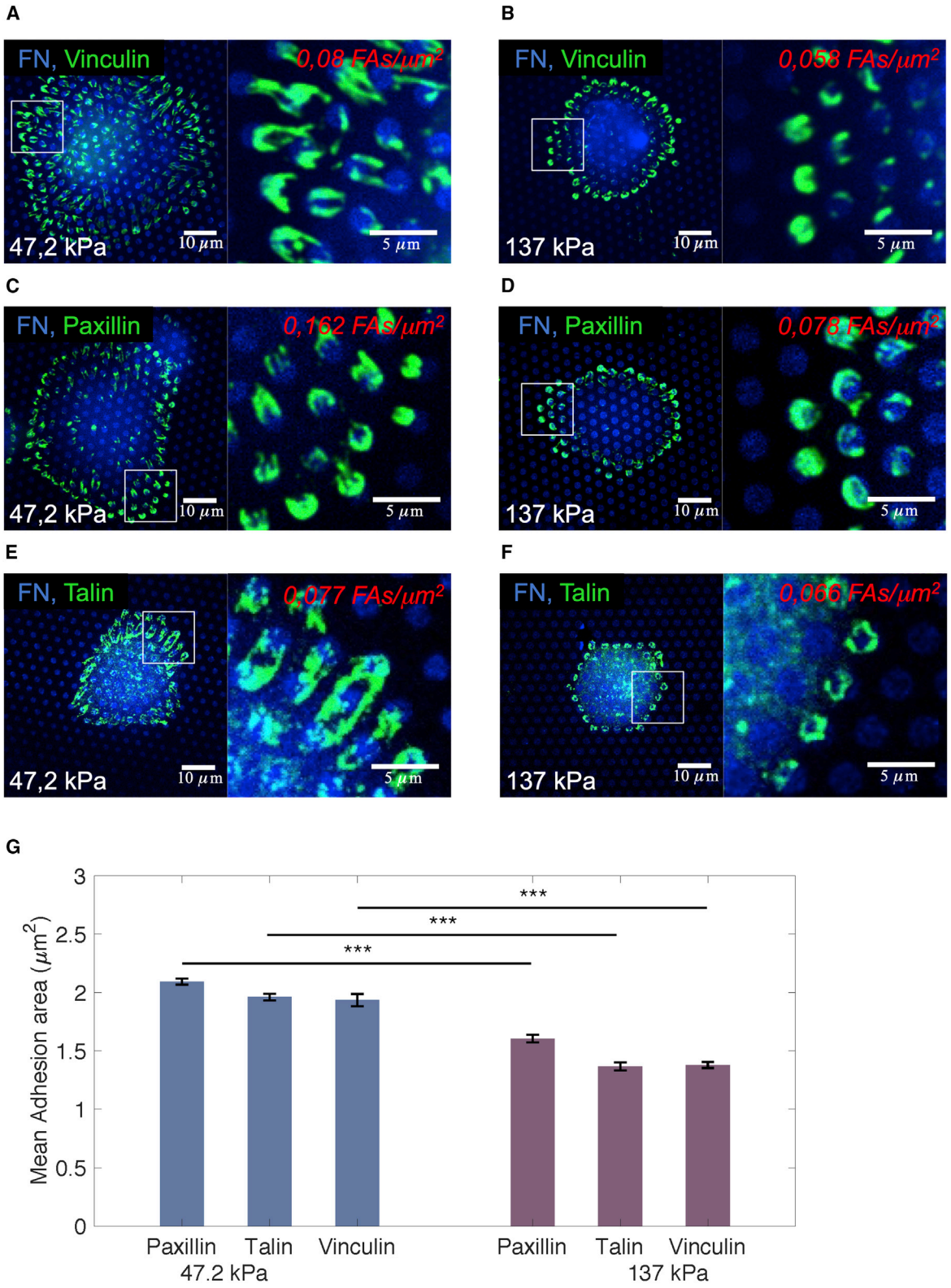

(legend on next page)

upper pillar surface, were thoroughly passivated by Pluronic, effectively preventing cell attachment. Indeed, the F-actin rings observed below the upper surface of stiff pillars were not supported by cell-matrix adhesions. A 3D analysis of the location of the different components showed that, on stiff pillar arrays, actin fibers (green) were ~1.5 μm below the FN-coated (blue) pillar tops, whereas cell-matrix adhesion components (vinculin, red) were exclusively localized at the upper surface (Figure 5A). By contrast, on pillar arrays of intermediate stiffness, FN, vinculin, and F-actin all coincided within 0.8 μm at the upper pillar surface.

To analyze the role of cytoskeletal tension and cellular traction force application in relation to the switch in cytoskeletal organization on stiff substrates, PCs were treated with a low concentration (0.5 μM) of the ROCK inhibitor Y-27632. ROCK inhibition led to an increased spreading area of PCs on soft as well as stiff substrates, while the cell area on pillars of intermediate stiffness was hardly affected (Figure 6A). This indicated that the spreading area was limited by strong cellular contractile forces on soft and stiff substrates. Indeed, traction forces on stiff micropillars, but not on pillars of intermediate stiffness, were suppressed by a factor of ~1.2 in the presence of Y-27632 (Figure 6B). Moreover, the reduction of traction forces caused by ROCK inhibition was accompanied by loss of the ring-like structures surrounding pillars (Figure 6C) and reversal of PC cytoskeletal morphology to parallel F-actin stress fibers located on top of the pillar arrays (Figure 6D).

Suppression of PC Spreading on 2D Patterned FN Substrates of High and Low Stiffness

We next investigated whether the switch in cytoskeletal organization and the suppression of cell spreading on stiff micropillars was determined by the 3D topography of the micropillar arrays. For this purpose, 2D micropatterned substrates were designed, which consisted of FN spots within an LM monolayer on a flat surface whose stiffness could be varied, ranging from 3.6 to 250 kPa. As surface, we utilized hPAAm hydrogels that provide the same flexibility in substrate micropatterning as PDMS gels, but allow more precise stiffness modulation (Grevesse et al., 2013). Flat PDMS stamps were generated and coated with a layer of LM-111 containing a hexagonal pattern of 2-μm-wide holes of 2-μm spacing, which was covered by an FN monolayer, creating a double layer of LM and FN. This stamp was subsequently inverted onto the hPAAm hydrogels of varying stiffness to print a pattern of FN spots embedded in LM similar to the geometry described in Figure 1B (Figure 7A). The stiffness of the hPAAm substrate was varied between 3.6 and 250 kPa, a stiffness range within what has been described for blood vessels (Balooch et al., 1998; Grant and Twigg, 2013; Hemmasizadeh et al., 2012; Kohn et al., 2015).

PCs were seeded onto these flat micropatterned substrates and fixed after 4 h of incubation. As observed for the pillar arrays, the spreading area followed a bell-shaped curve with low spreading at low and high stiffness, and increased spreading at intermediate stiffness. The spreading area doubled to its maximum value at 25 kPa (1,200 ± 60 μm^2 on 3.6 kPa versus 2,500 ± 120 μm^2 on 25 kPa), and decreased at high stiffness (1,600 ± 80 μm^2 on 40 kPa) (Figure 7C). The cell spreading area on micropatterned hPAAm gels up to 250 kPa was still significantly lower than that observed on a continuous substrate of non-physiological stiffness, such as PDMS (1 MPa) and glass (1 GPa) (Figure 7D). The preference of PCs to attach to FN over LM was again seen on micropatterned hPAAm substrates. Areas covered with LM were less distorted than areas covered with FN indicating a preferential force application on FN-covered areas (Figure 7B). Furthermore, on gels with a stiffness >40 kPa, the extracellular matrix coating was disrupted from the surface, further indicating the high forces applied by PCs at high substrate stiffness (Figure 7B).

DISCUSSION

PCs have been implicated in regulation of microvessel blood flow and capillary diameter in health and disease. Thus, the mechanical PC-endothelium interaction represents a potential target for therapy. However, it is not understood whether PCs actively and directly participate in control of the vascular diameter, nor is it understood how a putative mechanical connection between PCs and ECs is regulated. N-Cadherin-mediated binding of PCs to ECs

Figure 4. Cell-Matrix Adhesion Area of PCs (dif31) Placed on PDMS Micropillar Arrays of High (137 kPa) and Intermediate (47.2kPa) Stiffness

(A–F) Confocal immunofluorescence images of PCs (dif31) seeded on PDMS micropillar arrays of two different stiffness (137 and 47.2 kPa), functionalized with FN (blue). Cells were stained for vinculin (A and B), paxillin (C and D), and talin (E and F) (green).

(G) Average cell-matrix adhesion area of PC cells on PDMS micropillar arrays with 137 kPa stiffness (right) and 47.2 kPa (left), after 4 h of incubation. All error bars are SEM derived from two independent experiments performed with a minimum of two replicates. At least 30 cells were analyzed from each sample. NS, $p > 0.05$, *$p < 0.05$, **$p < 0.005$, ***$p < 0.0005$ according to the Mann-Whitney test. See also Figure S3.

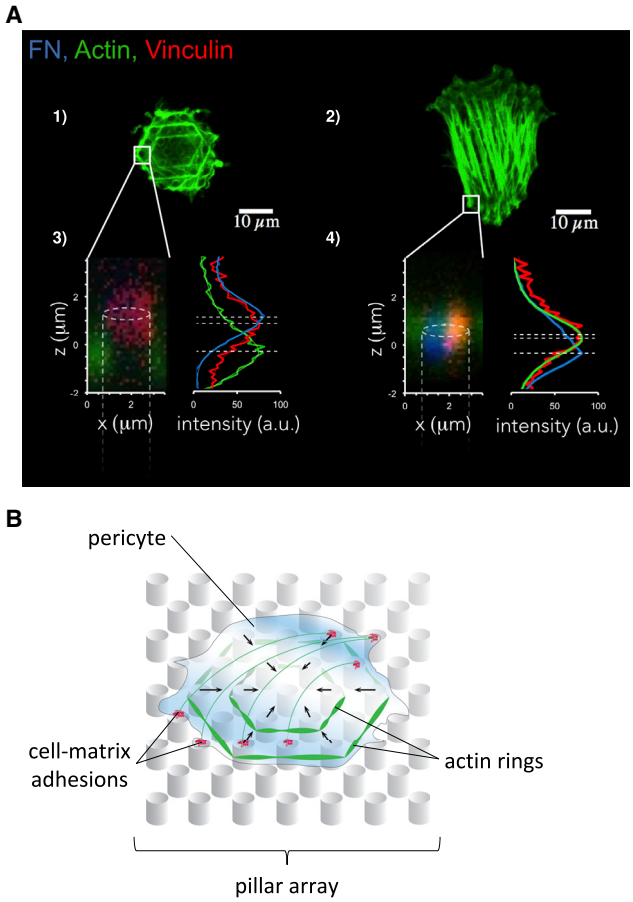

Figure 5. Differential Actin Cytoskeleton Organization of PCs

(A) Confocal images of the PC (dif31) actin cytoskeleton organization on (1) 137-kPa and (2) 47.2-kPa pillars. (A) 3) and 4) on the left, z projections of the boxed area showing actin (green) and vinculin (red) localization relatively to FN-coated (blue) micropillars; on the right, intensity profiles of the z projections, normalized to 100.

(B) Schematic representation of the PC actin cytoskeleton organization on stiff micropillars.

See also Figure S4.

is important during angiogenesis (Gerhardt et al., 2000), yet N-cadherin expression by ECs is downregulated with vessel maturation and BM formation (Ferreri et al., 2008; Gerhardt et al., 1999). Therefore, adhesion to the BM represents the most likely connection between PCs and ECs in mature, resting capillaries. The BM has a complex composition. Earlier studies pointed to a particular role for small FN deposits embedded in the LM-rich BM for PC adhesion (Courtoy and Boyles, 1983).

Our results support the role of FN deposits in PC interaction with the BM. By modeling FN deposits and their mechanical properties in different ways, we show that PCs have a strong preference toward FN over LM. PCs organize their cell-matrix adhesions mainly on FN while avoiding LM. PCs are guided by thin stripes of FN dots embedded in an LM layer. Interestingly, in the BM of tumor capillaries, FN is frequently overexpressed and is not organized as small distributed patches, but as a thick homogeneous layer (Zhou et al., 2008). This has been shown to be accompanied by a loose association between PCs and ECs, the opening of spaces separating the two cell types, and the formation of long PC protrusions into the tumor parenchyma, all resulting in wide, leaky microvessels (Morikawa et al., 2002). Similar effects were reported in the complete absence of FN (Stratman et al., 2009). Nevertheless, PCs can also leave ECs in injury or normal development conditions and act as progenitor/stem cells (Dellavalle et al., 2011; Dulauroy et al., 2012; Feng et al., 2011; Winkler et al., 2011). Notably, in PC-EC co-cultures, FN expression was found to be upregulated in ECs, yet downregulated in PCs (Stratman et al., 2009), implying that FN in the capillary BM originates mainly from ECs. Hence, it is conceivable that a tight crosstalk between ECs and PCs exists, which orchestrates the formation of an LM-rich BM containing small FN deposits. Altogether, our work and the previous findings point to a critical role for the organization of FN deposits in the LM-rich BM for PC adhesion and microvascular function.

Our data provide evidence that capillary FN deposits can serve as points for PC mechanosensing and mechanotransduction. PCs respond to the variation in FN-patterned substrate stiffness with changes in force application, spreading, and cell-matrix adhesions size. PCs show optimal spreading on intermediate (20–40 kPa) substrate stiffness, whereas the spreading area was suppressed on both soft and stiff, which is paralleled by an increased size of cell-matrix adhesions on intermediate stiffness substrates. Such mechanoresponsive behavior aligns with the "molecular-clutch hypothesis" (Alberto et al., 2018), which assumes that a response to mechanical cues decreases below or above an optimal rigidity by an increase in the molecular unbinding rate. The increased unbinding would result in lower cell forces, smaller cell substrate adhesions, and an ineffective cell spreading on very soft and very rigid matrices. The molecular-clutch model faithfully describes the mechanoresponse of neuronal growth cones and glioma cells (Alberto et al., 2018; Bangasser et al., 2017; Chan and Science, 2008). Remarkably, we find that forces applied by PCs on intermediate stiffness substrates are lower than on soft or stiff substrates, which differs from earlier observations with other, in particular fibroblastic, cell types (Ghibaudo et al., 2008; Han et al., 2012). Our own direct comparison with human and mouse fibroblasts where cellular traction forces gradually increase with increasing substrate stiffness corroborate those findings. Another prediction of the molecular-clutch model is the cellular response to suppression of myosin activity (Alberto

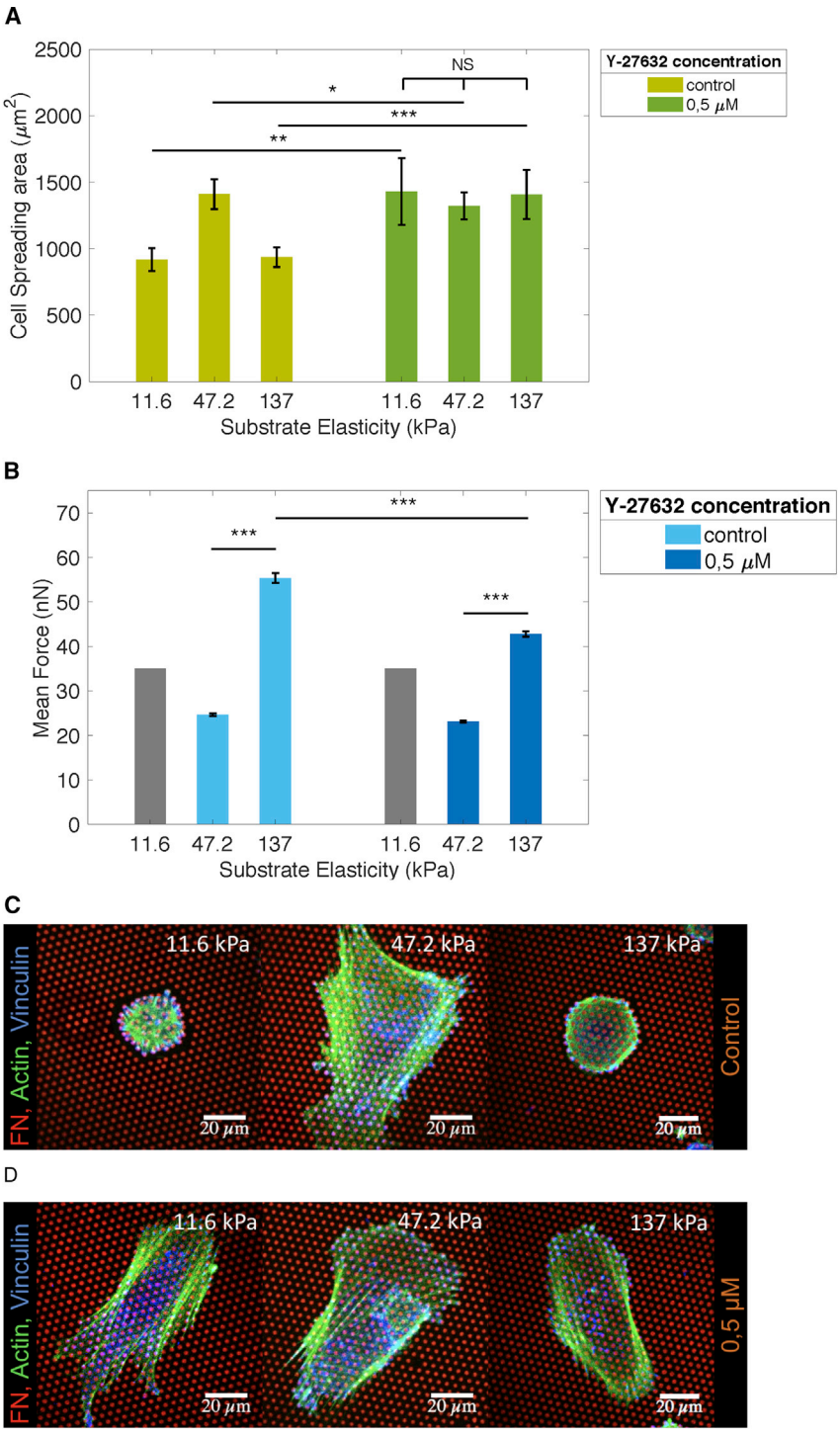

Figure 6. Inhibition of ROCK Alters PC Spreading on Stiff (137 kPa) and Soft (11.6 kPa) PDMS Micropillar Arrays

(A) Average PC (dif31) spreading area without (left) and with (right) Y-27632 (0.5 μM) after 4 h of incubation.

(B) Average PC (dif31) forces, respectively.

(C and D) Representative immunofluorescence images of PC (dif31) spreading and actin cytoskeleton organization (green) on PDMS micropillars (red) without Y-27632 (C) and with 0.5 μM Y-27632 (D) after 4 h of incubation. All error bars are SEM derived from two independent experiments performed with a minimum of two replicates. At least 30 cells were analyzed from each sample.

NS, $p > 0.05$, *$p < 0.05$, **$p < 0.005$, ***$p < 0.0005$ according to the Mann-Whitney test.

et al., 2018). Indeed, we observe that mild ROCK inhibition, which would attenuate force generation, improves PC spreading on stiff and soft substrates.

The high forces and small spreading area observed for PCs on stiff micropillar arrays were accompanied by a dramatic change in cytoskeletal F-actin organization. In comparison with the linear organization of stress fibers on intermediate stiffness pillars, PCs formed circular F-actin rings surrounding very stiff micropillar arrays. Cell-matrix adhesions assembled on the FN-coated surface of

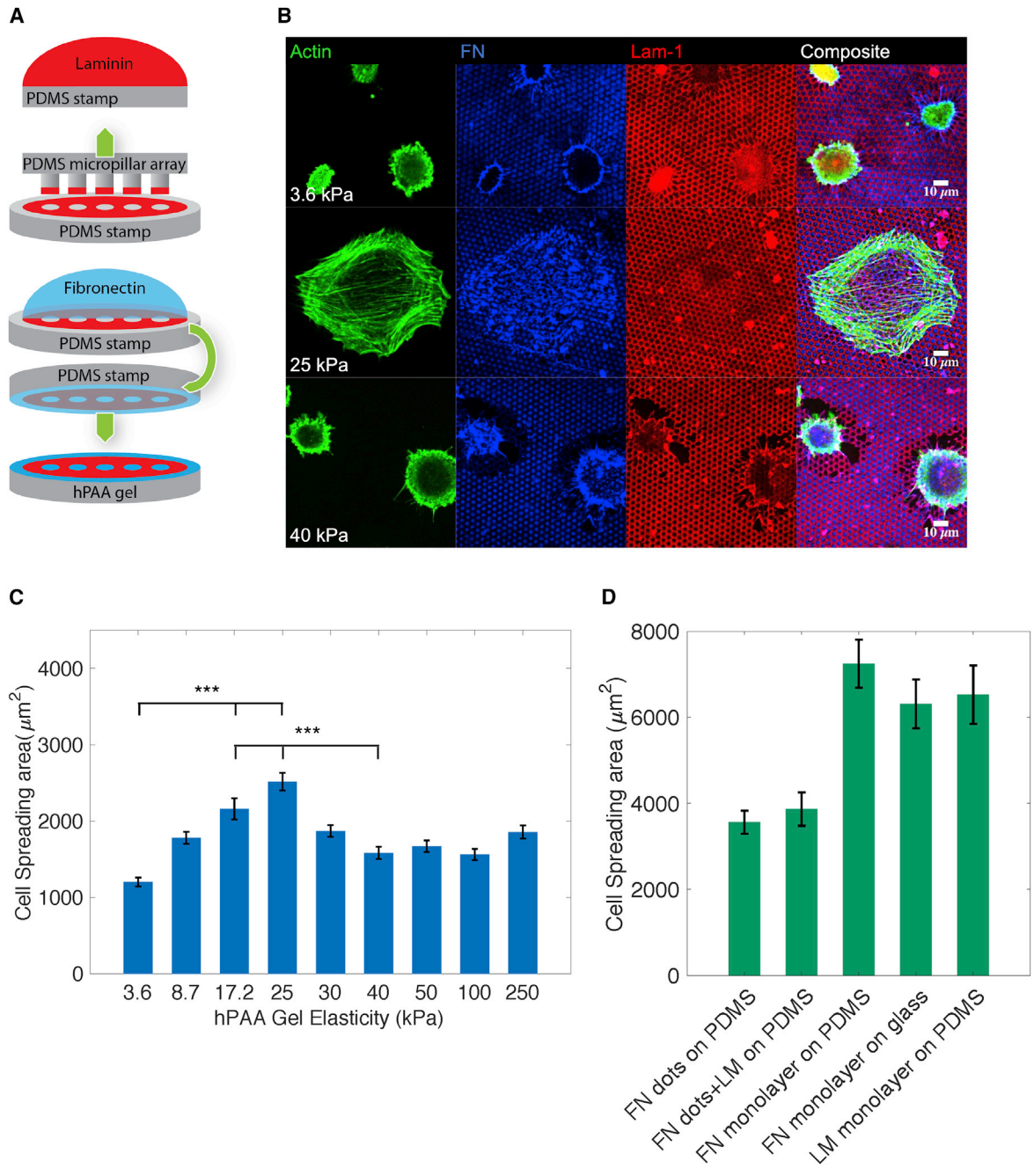

Figure 7. PCs (dif31) Spreading on Hydroxy-PAAm Hydrogels of Different Stiffness

(A) Microcontact printing scheme of hPAAm hydrogels with FN spots surrounded by LM-111.

(B) Representative immunofluorescence images of PCs (dif31) seeded on hydroxy-PAAm hydrogels of 3.6, 25, and 40 kPa stiffness (from top to bottom).

(C) Average PC (dif31) spreading area on a palette of hydroxy-PAAm hydrogels with different stiffness and FN and LM stamping.

(D) PCs (dif31) spreading on PDMS flat surfaces stamped with: (1) FN dots, (2) FN dots surrounded by LM-111, (3) FN monolayer, and (4) LM-111 monolayer; and glass coated with FN monolayer. All surfaces were blocked with BSA 1%. All error bars are SEM derived from three independent experiments performed with a minimum of two replicates. At least 30 cells were analyzed from each sample. NS, $p > 0.05$, *$p < 0.05$, **$p < 0.005$, ***$p < 0.0005$ according to the Mann-Whitney test.

such pillar arrays, but the actin-ring structures encircled multiple pillars below the pillar tops. We hypothesize that such engulfing through ring-like F-actin cytoskeleton organization could represent a cell adaptation process toward the "frictional slippage" regime described earlier (Elosegui-Artola et al., 2016), allowing PCs to increase forces on substrates outside their optimal rigidity. In line with this hypothesis, we found that mild ROCK inhibition reversed the change in F-actin cytoskeletal organization back to an organization as observed on intermediate stiffness.

The use of flat hPAAm hydrogels instead of PDMS micropillars, allowed us to eliminate the effect of substrate topography while keeping the opportunity to tune the substrate stiffness. On flat 2D micropatterned surfaces the PC behavior was similar to that found on micropillar arrays: PCs showed optimal spreading on intermediate stiffness substrates. Yet, we noticed that the optimal stiffness for PC spreading differed on hPAAm hydrogels (25 kPa) to that on PDMS micropillar arrays (47 kPa). This small, yet significant, difference is likely due to the 2D versus 3D geometry of the substrates, the tightly restricted area for cell-matrix adhesions on the micropillar arrays, and/or the absence of LM in the micropillar model system. Interestingly, for micropatterned hydrogel substrates, the stiffness range of 15–25 kPa supporting optimal PC spreading was close to that determined by atomic force microscopy for ECs and smooth muscle cells (Hong et al., 2015; Okamoto et al., 2017), indicating that this stiffness range represents a response in a physiologically relevant stiffness regime. Behavior of PCs observed in this study may provide an insight on the way PCs distinguish deviations of the microvessel stiffness from the normal and react by increasing contractile forces. A limitation of this study is the unavailability of *ex-vivo*-isolated mid-capillary PCs. We derived CD31- PCs from an hiPSC line and used different differentiations. Robustness of PC behavior described here could be further increased using PCs derived from multiple independent hiPSC lines in future studies.

Taken together, our study shows that PCs strongly prefer FN over LM, that PCs recognize and align to FN dots within an LM substrate, that PCs apply forces to FN deposits, and that PCs are able to sense variations in mechanical properties of the FN deposits and respond to this by changing traction force, cell spreading area, and the size of cell-matrix adhesions. Our findings also point to a mechanoresponsive behavior of PCs that significantly differs from that observed for fibroblasts and other cell types. Our findings support a role for FN deposits in the BM as adhesion points for mechanoregulation of the microvasculature by PCs. Our *in vitro* model system of micropillar arrays/micropatterned hydrogels in combination with hiPSC-derived PCs described earlier (Dar et al., 2012; Orlova et al., 2014b) can be a valuable testbed to study the mechanisms of PC force regulation in physiology and pathology under well-controlled conditions and may serve as a model for drug discovery efforts.

EXPERIMENTAL PROCEDURES

Cell Culture

CD31- hiPSC line LUMC06iCTRL-derived PCs (Dambrot et al., 2013; Orlova et al., 2014b) (dif31 and dif43) and SV80 human fibroblasts cells were cultured in Dulbecco's modified Eagle's medium (DMEM) (Gibco/Thermo Fisher Scientific, USA) supplemented with 10% fetal bovine serum (HyClone, Etten-Leur, the Netherlands), 25 U/mL penicillin, and 25 μg/mL streptomycin (Invitrogen/Fisher Scientific). NIH3T3 mouse fibroblasts were cultured in DMEM (Sigma) supplemented with 10% calf serum (Thermo Scientific/Sigma), 2 mM glutamine, and 100 μg/mL penicillin/streptomycin. For all experiments cells were seeded at 20,000 cells directly on the patterned surface. After 4 h of incubation they were fixed for 10 min in 4% paraformaldehyde in PBS for immunostaining.

Immunostaining

After cells were fixed, they were permeabilized for 10 min with 0.1% Triton X and blocked for 1 h with 1% BSA (Sigma, a2153) in PBS. For cell-matrix adhesion assays after 4 h of incubation, cells were washed in cytoskeleton buffer (CB), incubated 15 s in 0.1%–0.25% Triton X, 0.4% paraformaldehyde, and 1 μg/mL phalloidin in CB, washed again with CB, and fixed for 10 min with 4% paraformaldehyde in CB. Finally, they were permeabilized for 10 min with 0.5% Triton X and blocked for 1 h with 1% BSA in PBS. Immunostaining was done depending on the experiment, with Alexa 532 phalloidin—1:500 stock concentration in PBS over 30 min (Thermo Fisher Scientific, a22282) or primary antibodies against paxillin (Thermo Fisher Scientific, aho0492), talin (Sigma, t3287), vinculin (Sigma, v9131), alpha-v integrin (Merck Millipore, mab1978), beta-1 integrin (Santa Cruz, sc-18887) with 1:200 stock concentration, or LM-111 with 1:500 stock concentration in 1% BSA in PBS over 2 h (Sigma, l9393), followed with Alexa 532 or Alexa 647-conjugated secondary antibodies against mouse immunoglobulin G (IgG) with 1:200 stock concentration (Thermo Fisher Scientific, a11002 and Jackson, 115-605-006, respectively) and Alexa 647-conjugated secondary antibody against rabbit IgG with 1:500 stock concentration in 1% BSA in PBS over 2 h (Thermo Fisher Scientific, a21244).

PDMS Surface Patterning with FN and LM

PDMS surface with 2,300 kPa stiffness and a pattern, where LM surrounds FN spots or inverse, was produced by combining stamp-off and microcontact printing methods (Desai et al., 2014). Two flat PDMS (Sylgard 184, Dow Corning) 1:30 (crosslinker:prepolymer ratio, cured 16 h at 65°C) stamps were separately incubated for 60 min with a 40-μL drop of 50 μg/mL LM-111 (Sigma, l2020) in Milli-Q water and a 40 μL mixture of 50 μg/mL FN (Sigma, f1141) plus 10 μg/mL Alexa 405-FN in Milli-Q, washed with Milli-Q and dried under laminar flow. Using UV-Ozone-activated PDMS 1:10 micropillar arrays, where 2-μm-diameter pillars with

2-μm spacing and hexagonal order, we obtained holes in one of the layers. Furthermore, two stamps were inverted one-by-one on top of the UV-Ozone-activated PDMS 1:10 surface and incubated for 10 min each, to get a previously modified protein sheet on top of the uninterrupted layer of the second (Figures 1B and 1C).

PDMS surfaces with a grid of crossing FN and LM lines were obtained in a similar manner. First, two PDMS 1:10 molds with 5-μm-high lines of different width were produced using replica molding from a silicon wafer. After UV-Ozone activation for 10 min, they were pushed onto PDMS 1:30 stamps with a protein layer dried on them. Following 10 min of incubation and removal, this mold left a negative of the pattern in the protein layer on top of the PDMS stamps. Furthermore, PDMS stamps were inverted on top of the UV-Ozone-activated PDMS 1:10 surface, creating a pattern of crossing LM and FN lines on it (Figure 2A).

PDMS surfaces with FN lines under a layer of LM with holes were printed using PDMS stamps with LM and FN layers modified as mentioned previously. The PDMS micropillar array was used to make holes in the dry LM monolayer and the PDMS mold with lines was used to create a line pattern in FN. Furthermore, these stamps were loaded on top of the UV-Ozone-activated PDMS surface, with the FN stamp going first (Figure 2B).

Finally, all patterned PDMS surfaces were blocked for 1 h with 1% BSA.

PDMS Micropillar Array Preparation

PDMS micropillar arrays were prepared as was described previously (van Hoorn et al., 2014; du Roure et al., 2005). In brief, an Si master mold was made using a two-step deep reactive ion etching process. This yielded a 10 × 10-mm hexagonal array of 2-μm-diameter holes with 2-μm spacing and varying depth, flanked by two 50-μm-deep 10 × 2-mm tranches. After mold passivation with trichloro silane (Sigma), PDMS 1:10 was poured over it and cured for 20 h at 110°C. The peeled off PDMS had a negative of the mold shape with micropillar array and 50-μm-high spacers on the sides of it. This array was functionalized with the help of PDMS 1:30 stamps and dried protein of interest on top of them. A 40-μL drop of FN or LM-111 mixture in water was incubated for 60 min on the PDMS 1:30 stamp, then washed and dried under laminar flow. This stamp was then gently loaded onto UV-Ozone-activated PDMS micropillar array for 10 min. Finally, stamped array was blocked with 0.2% Pluronic (F-127, Sigma) in PBS for 60 min at room temperature and washed with PBS.

Hydroxy-Polyacrylamide Gel Preparation

Hydroxy-polyacrylamide (HPAAm) hydrogels were made following a previously described method (Grevesse et al., 2013). Gels stiffer than 40 kPa were obtained by increasing polyacrylamide monomer concentration with a fixed monomer/crosslinker ratio of 29:1 following a procedure reported earlier (Grevesse et al., 2015; Jiang et al., 2007). Furthermore, gels were stamped with an LM and FN pattern where FN spots were surrounded by LM. This was achieved by using adapted stamp-off and microcontact printing approaches as described by Desai et al. (2014). A 40-μL drop of 50 μg/mL LM-111 in Milli-Q water was incubated for 60 min on top of the 10 × 10-mm PDMS 1:30 stamp, followed by washing and drying under laminar flow. Then the UV-Ozone-activated PDMS micropillar array was pushed onto the dry LM-111 monolayer to obtain holes in the places of micropillar-LM-111 contacts. After 10 min of incubation the array was removed and a second 40-μL drop of 50 μg/mL FN plus 10 μg/mL Alexa 405-FN in Milli-Q was gently spread onto the first layer for 1 h. Finally, the stamp was washed and dried under laminar flow. HPAAm hydrogels were dried using nitrogen flow and incubated with the stamp for 1 h (Figure 7A), following blocking with 1% BSA in PBS o/n and washing with PBS.

Microscopy

Confocal imaging was performed on a home-built setup based on an Axiovert 200 microscope body (Zeiss), spinning disk unit (CSU-X1, Yokogawa), and an em-CCD camera (iXon 897, Andor). IQ software enabled setup control and data acquisition. Lasers of 405 nm (CrystaLaser), 488 nm (Coherent), 514 nm, 561 nm (Cobolt), and 642 nm (Spectra Physics) wavelengths were coupled into the CSU via a polarization-maintaining single-mode fiber. Spacers on the sides of the micropillar arrays allowed placing them upside down onto #0 coverslips (Menzel Glaser) with adhered cells facing down. This approach ensured reproducible cell observation within the limited working distance of a high NA objective on an inverted microscope. For PDMS and hPAAm 2D assays parafilm spacers were made directly on top of the glass coverslips.

Image Analysis

Cell spreading area was quantified using FIJI software. First the background was subtracted by adjusting the threshold level, followed by the cell edge selection with a tracing tool. Finally, the mean values for at least 30 cells per condition were calculated.

Cell traction forces were measured by using micropillar array technology (Tan et al., 2003; du Roure et al., 2005; Fu et al., 2010) and quantified as described previously (van Hoorn et al., 2014). Micropillar tops were functionalized with fluorescently labeled FN or LM with further immunostaining. This allowed us to detect deflections with ~30 nm accuracy, which corresponded to a force precision of 500 pN for soft and 2 nN for stiff pillars, respectively. Analysis was performed using a specifically designed MATLAB script.

The cell-matrix adhesion area was determined as described by Balcioglu et al. (2015). Fluorescent images of cell-matrix adhesion proteins were passed through a Gaussian lowpass filter, followed by a hole-filling algorithm and watershed-segmentation. All results were manually controlled to remove images with incorrect adhesion-detection due to a low signal-to-noise ratio.

Statistical Analysis

To assess significance of the difference between two conditions, the Wilcoxon rank-sum test was used. This test is an equivalent to a Mann-Whitney U-test. The significance for the force application by PCs represented in graph 3E was quantified using an ANOVA test comparing means of the mean values determined for at least three independent experiments per each stiffness.

SUPPLEMENTAL INFORMATION

Supplemental Information can be found online at https://doi.org/10.1016/j.stemcr.2020.05.001.

AUTHOR CONTRIBUTIONS

O.I. carried out the experiments. O.I., E.H.J.D., and T.S. wrote the manuscript. V.V.O. and C.L.M. provided IPS-derived pericytes, assistance with pericyte culture, and critically read the manuscript. T.S. and E.H.J.D. supervised the project.

ACKNOWLEDGMENTS

We thank Dr. Sylvain Gabriele and Dr. Joséphine Lantoine, University of Mons, Belgium, for their help in setting up hPAAm gel experiments for this paper. This work is part of the research programme Mechanosensing and Mechano-transduction by Cells (MMC09) financed by the Dutch Research Council (NWO).

Received: April 28, 2019
Revised: April 30, 2020
Accepted: May 1, 2020
Published: May 28, 2020

REFERENCES

Alberto, E., Trepat, X., and Pere, R. (2018). Control of mechanotransduction by molecular clutch dynamics. Trends Cell Biol. *28*, 356–367.

Armulik, A., Abramsson, A., and Betsholtz, C. (2005). Endothelial/pericyte interactions. Circ. Res. *97*, 512–523.

Armulik, A., Genové, G., and Betsholtz, C. (2011). Pericytes: developmental, physiological, and pathological perspectives, problems, and promises. Dev. Cell *21*, 193–215.

Armulik, A., Genové, G., Mäe, M., Nisancioglu, M.H., Wallgard, E., Niaudet, C., He, L., Norlin, J., Lindblom, P., Strittmatter, K., et al. (2010). Pericytes regulate the blood-brain barrier. Nature *468*, 557–561.

Balaban, N.Q., Schwarz, U.S., Riveline, D., Goichberg, P., Tzur, G., Sabanay, I., Mahalu, D., Safran, S., Bershadsky, A., Addadi, L., and Geiger, B. (2001). Force and focal adhesion assembly: a close relationship studied using elastic micropatterned substrates. Nat. Cell Biol. *3*, 466–472.

Balcioglu, H., van Hoorn, H., Donato, D., Schmidt, T., and Danen, E. (2015). The integrin expression profile modulates orientation and dynamics of force transmission at cell-matrix adhesions. J. Cell Sci. *128*, 1316–1326.

Balooch, M., Wu-Magidi, I.C., Balazs, A., Lundkvist, A., Marshall, S., Marshall, G., Siekhaus, W., and Kinney, J. (1998). Viscoelastic properties of demineralized human dentin measured in water with atomic force microscope (AFM)-based indentation. J. Biomed. Mater. Res. *40*, 539–544.

Bangasser, B.L., Shamsan, G.A., Chan, C.E., Opoku, K.N., Tüzel, E., Schlichtmann, B.W., Kasim, J.A., Fuller, B.J., McCullough, B.R., Rosenfeld, S.S., and Odde, D.J. (2017). Shifting the optimal stiffness for cell migration. Nat. Commun. *8*, 15313.

Bell, R.D., Winkler, E.A., Sagare, A.P., Singh, I., Barb, L., Deane, R., and Zlokovic, B.V. (2010). Pericytes control key neurovascular functions and neuronal phenotype in the adult brain and during brain aging. Neuron *68*, 409–427.

Chan, C., and Science, O.D. (2008). Traction dynamics of filopodia on compliant substrates. Science *322*, 1687–1691.

Courtoy, P., and Boyles, J. (1983). Fibronectin in the microvasculature: localization in the pericyte-endothelial interstitium. J. Ultrastruct. Res. *83*, 258–273.

Dambrot, C., Pas, S., Zijl, L., Brändl, B., Wang, J., Schalij, M., Hoeben, R., Atsma, D., Mikkers, H., Mummery, C., and Freund, C. (2013). Polycistronic lentivirus induced pluripotent stem cells from skin biopsies after long term storage, blood outgrowth endothelial cells and cells from milk teeth. Differentiation *85*, 101–109.

Dar, A., Domev, H., Oren, B., Tzukerman, M., Naama, Z., Novak, A., Germanguz, I., Amit, M., and Joseph, I. (2012). Multipotent vasculogenic pericytes from human pluripotent stem cells promote recovery of murine ischemic limb. Circulation *125*, 87–99.

Dellavalle, A., Maroli, G., Covarello, D., Azzoni, E., Innocenzi, A., Perani, L., Antonini, S., Sambasivan, R., Brunelli, S., Tajbakhsh, S., and Cossu, G. (2011). Pericytes resident in postnatal skeletal muscle differentiate into muscle fibres and generate satellite cells. Nat. Commun. *2*, 499.

Desai, R.A., Rodriguez, N.M., and Chen, C.S. (2014). Stamp-off to micropattern sparse, multicomponent features. Methods Cell Biol. *119*, 3–16.

du Roure, O., Saez, A., Buguin, A., Austin, R.H., Chavrier, P., Silberzan, P., Siberzan, P., and Ladoux, B. (2005). Force mapping in epithelial cell migration. Proc. Natl. Acad. Sci. U S A *102*, 2390–2395.

Dulauroy, S., Carlo, S., Langa, F., Eberl, G., and Peduto, L. (2012). Lineage tracing and genetic ablation of ADAM12+ perivascular cells identify a major source of profibrotic cells during acute tissue injury. Nat. Med. *18*, 1262.

Elosegui-Artola, A., Oria, R., Chen, Y., Kosmalska, A., Perez-Gonzalez, C., Castro, N., Zhu, C., Trepat, X., and Roca-Cusachs, P. (2016). Mechanical regulation of a molecular clutch defines force transmission and transduction in response to matrix rigidity. Nat. Cell Biol. *18*, 540–548.

Feng, J., Mantesso, A., Bari, C., Nishiyama, A., and Sharpe, P. (2011). Dual origin of mesenchymal stem cells contributing to organ growth and repair. Proc. Natl. Acad. Sci. U S A *108*, 6503–6508.

Ferreri, D.M., Minnear, F.L., Yin, T., Kowalczyk, A.P., and Vincent, P.A. (2008). N-Cadherin levels in endothelial cells are regulated by monolayer maturity and p120 availability. Cell Commun. Adhes. *15*, 333–349.

Fu, J., Wang, Y.K., Yang, M.T., Desai, R.A., Yu, X., Liu, Z., and Chen, C.S. (2010). Mechanical regulation of cell function with geometrically modulated elastomeric substrates. Nat. Methods *7*, 733–736.

Fujimoto, K. (1995). Pericyte-endothelial gap junctions in developing rat cerebral capillaries: a fine structural study. Anat. Rec. *242*, 562–565.

Gerhardt, H., Liebner, S., Redies, C., and Wolburg, H. (1999). N-Cadherin expression in endothelial cells during early angiogenesis

in the eye and brain of the chicken: relation to blood-retina and blood-brain barrier development. Eur. J. Neurosci. *11*, 1191–1201.

Gerhardt, H., Wolburg, H., and Redies, C. (2000). N-Cadherin mediates pericytic-endothelial interaction during brain angiogenesis in the chicken. Dev. Dyn. *218*, 472–479.

Ghibaudo, M., Saez, A., Trichet, L., Xayaphoummine, A., Browaeys, J., Silberzan, P., Buguin, A., and Ladoux, B. (2008). Traction forces and rigidity sensing regulate cell functions. Soft Matter, 1836–1843. https://doi.org/10.1039/B804103B.

Grant, C., and Twigg, P. (2013). Pseudostatic and dynamic nanomechanics of the tunica adventitia in elastic arteries using atomic force microscopy. ACS Nano *7*, 456–464.

Grevesse, T., Dabiri, B.E., Parker, K., and Gabriele, S. (2015). Opposite rheological properties of neuronal microcompartments predict axonal vulnerability in brain injury. Sci. Rep. *5*, 9475.

Grevesse, T., Versaevel, M., Circelli, G., Desprez, S., and Gabriele, S. (2013). A simple route to functionalize polyacrylamide hydrogels for the independent tuning of mechanotransduction cues. Lab Chip *13*, 777–780.

Halfter, W., Monnier, C., Müller, D., Oertle, P., Uechi, G., Balasubramani, M., Safi, F., Lim, R., Loparic, M., and Henrich, P.B. (2013). The bi-functional organization of human basement membranes. PLoS One *8*, e67660.

Hall, A.P. (2006). Review of the pericyte during angiogenesis and its role in cancer and diabetic retinopathy. Toxicol. Pathol. *34*, 763–775.

Hall, C.N., Reynell, C., Gesslein, B., Hamilton, N.B., Mishra, A., Sutherland, B.A., O'Farrell, F.M., Buchan, A.M., Lauritzen, M., and Attwell, D. (2014). Capillary pericytes regulate cerebral blood flow in health and disease. Nature *508*, 55–60.

Hamilton, N.B., Attwell, D., and Hall, C.N. (2010). Pericyte mediated regulation of capillary diameter: a component of neurovascular coupling in health and disease. Front. Neuroenergetics *2*. https://doi.org/10.3389/fnene.2010.00005.

Han, S.J., Bielawski, K.S., Ting, L.H., Rodriguez, M.L., and Sniadecki, N.J. (2012). Decoupling substrate stiffness, spread area, and micropost density: a close spatial relationship between traction forces and focal adhesions. Biophys. J. *103*, 640–648.

Hemmasizadeh, A., Autieri, M., and Darvish, K. (2012). Multilayer material properties of aorta determined from nanoindentation tests. J. Mech. Behav. Biomed. Mater. *15*, 199–207.

Hill, R.A., Tong, L., Yuan, P., Murikinati, S., Gupta, S., and Grutzendler, J. (2015). Regional blood flow in the normal and ischemic brain is controlled by arteriolar smooth muscle cell contractility and not by capillary pericytes. Neuron *87*, 95–110.

Hong, Z., Reeves, K., Sun, Z., Li, Z., Brown, N., and Meininger, G. (2015). Vascular smooth muscle cell stiffness and adhesion to collagen I modified by vasoactive agonists. PLoS One *10*, e0119533.

Jiang, X., Georges, P.C., Li, B., Du, Y., Kutzing, M.K., Previtera, M.L., Langrana, N.A., and Firestein, B.L. (2007). Cell growth in response to mechanical stiffness is affected by neuron-astroglia interactions. Open Neurosci. J. *1*, 7–14.

Joyce, N., Haire, M., and Palade, G. (1985a). Contractile proteins in pericytes. II. Immunocytochemical evidence for the presence of two isomyosins in graded concentrations. J. Cell Biol. *100*, 1387–1395.

Joyce, N., Haire, M., and Palade, G. (1985b). Contractile proteins in pericytes. I. Immunoperoxidase localization of tropomyosin. J. Cell Biol. *100*, 1379–1386.

Kisler, K., Nelson, A., Rege, S., Ramanathan, A., Wang, Y., Ahuja, A., Lazic, D., Tsai, P., Zhao, Z., Zhou, Y., et al. (2017). Pericyte degeneration leads to neurovascular uncoupling and limits oxygen supply to brain. Nat. Neurosci. *20*, 406–416.

Kohn, J.C., Lampi, M.C., and Reinhart-King, C.A. (2015). Age-related vascular stiffening: causes and consequences. Front. Genet. *6*, 112.

Le Beux, Y., and Willemot, J. (1978). Actin- and myosin-like filaments in rat brain pericytes. Anat. Rec. *190*, 811–826.

Mishra, A., Reynolds, J.P., Chen, Y., Gourine, A.V., Rusakov, D.A., and Attwell, D. (2016). Astrocytes mediate neurovascular signaling to capillary pericytes but not to arterioles. Nat. Neurosci. *19*, 1619–1627.

Morikawa, S., Baluk, P., Kaidoh, T., Haskell, A., Jain, R., and McDonald, D. (2002). Abnormalities in pericytes on blood vessels and endothelial sprouts in tumors. Am. J. Pathol. *160*, 985–1000.

Noberini, R., Mitra, S., Salvucci, O., Valencia, F., Duggineni, S., Prigozhina, N., Wei, K., Tosato, G., Huang, Z., and Pasquale, E.B. (2011). PEGylation potentiates the effectiveness of an antagonistic peptide that targets the EphB4 receptor with nanomolar affinity. PLoS One *6*, e28611.

Okamoto, T., Kawamoto, E., Takagi, Y., Akita, N., Hayashi, T., Park, E., Suzuki, K., and Shimaoka, M. (2017). Gap junction-mediated regulation of endothelial cellular stiffness. Sci. Rep. *7*, 6134.

Orlova, V.V., Drabsch, Y., Freund, C., Sandra, P., van den Hil, F.E., Muenthaisong, S., Dijke, P.T., and Mummery, C.L. (2014a). Functionality of endothelial cells and pericytes from human pluripotent stem cells demonstrated in cultured vascular plexus and zebrafish xenografts. Arterioscler. Thromb. Vasc. Biol. *34*, 177–186.

Orlova, V.V., van den Hil, F.E., Sandra, P., Drabsch, Y., Ten Dijke, P., and Mummery, C.L. (2014b). Generation, expansion and functional analysis of endothelial cells and pericytes derived from human pluripotent stem cells. Nat. Protoc. *9*, 1514–1531.

Paula, D., Katychev, A., Wang, X., and Van Buren, E. (2006). CNS microvascular pericytes exhibit multipotential stem cell activity. J. Cereb. Blood Flow Metab. *26*, 613–624.

Pelham, R., and Wang, Y. (1997). Cell locomotion and focal adhesions are regulated by substrate flexibility. Proc. Natl. Acad. Sci. U S A *94*, 13661–13665.

Peppiatt, C.M., Howarth, C., Mobbs, P., and Attwell, D. (2006). Bidirectional control of CNS capillary diameter by pericytes. Nature *443*, 700–704.

Salvucci, O., Maric, D., Economopoulou, M., Sakakibara, S., Merlin, S., Follenzi, A., and Tosato, G. (2009). EphrinB reverse signaling contributes to endothelial and mural cell assembly into vascular structures. Blood *114*, 1707–1716.

Stratman, A.N., Malotte, K.M., Mahan, R.D., Davis, M.J., and Davis, G.E. (2009). Pericyte recruitment during vasculogenic tube assembly stimulates endothelial basement membrane matrix formation. Blood *114*, 5091–5101.

Tan, J.L., Tien, J., Pirone, D.M., Gray, D.S., Bhadriraju, K., and Chen, C.S. (2003). Cells lying on a bed of microneedles: an approach to isolate mechanical force. Proc. Natl. Acad. Sci. U S A *100*, 1484–1489.

Tillet, E., Vittet, D., Féraud, O., Moore, R., Kemler, R., and Huber, P. (2005). N-Cadherin deficiency impairs pericyte recruitment, and not endothelial differentiation or sprouting, in embryonic stem cell-derived angiogenesis. Exp. Cell. Res. *310*, 392–400.

Trichet, L., Digabel, J., Hawkins, R., Vedula, S., Gupta, M., Ribrault, C., Hersen, P., Voituriez, R., and Ladoux, B. (2012). Evidence of a large-scale mechanosensing mechanism for cellular adaptation to substrate stiffness. Proc. Natl. Acad. Sci. U S A *109*, 6933–6938.

van Hoorn, H., Harkes, R., Spiesz, E.M., Storm, C., van Noort, D., Ladoux, B., and Schmidt, T. (2014). The nanoscale architecture of force-bearing focal adhesions. Nano Lett. *14*, 4257–4262.

Wallow, I., and Burnside, B. (1980). Actin filaments in retinal pericytes and endothelial cells. Invest. Ophthalmol. Vis. Sci. *19*, 1433–1441.

Winkler, E.A., Bell, R.D., and Zlokovic, B.V. (2011). Central nervous system pericytes in health and disease. Nat. Neurosci. *14*, 1398–1405.

Yemisci, M., Yasemin, G., Vural, A., Can, A., Topalkara, K., and Dalkara, T. (2009). Pericyte contraction induced by oxidative-nitrative stress impairs capillary reflow despite successful opening of an occluded cerebral artery. Nat. Med. *15*, 1031–1037.

Yeung, T., Georges, P.C., Flanagan, L.A., Marg, B., Ortiz, M., Funaki, M., Zahir, N., Ming, W., Weaver, V., and Janmey, P.A. (2005). Effects of substrate stiffness on cell morphology, cytoskeletal structure, and adhesion. Cell Motil. Cytoskeleton *60*, 24–34.

Yousif, L.F., Russo, J., and Sorokin, L. (2013). Laminin isoforms in endothelial and perivascular basement membranes. Cell Adh. Migr. *7*, 101110.

Zhou, X., Rowe, G.R., Hiraoka, N., George, J.P., Wirtz, D., Mosher, D.F., Virtanen, I., Chernousov, M.A., and Weiss, S.J. (2008). Fibronectin fibrillogenesis regulates three-dimensional neovessel formation. Genes Dev. *22*, 1231–1243.

Zimmermann, K. (1923). Der feinere Bau der Blutcapillaren. Z. Anat. Entwickl. *68*, 29–109.

Stem Cell Reports, Volume *14*

Supplemental Information

Fibronectin Patches as Anchoring Points for Force Sensing and Transmission in Human Induced Pluripotent Stem Cell-Derived Pericytes

Olga Iendaltseva, Valeria V. Orlova, Christine L. Mummery, Erik H.J. Danen, and Thomas Schmidt

Supplemental information

Figure S1

A

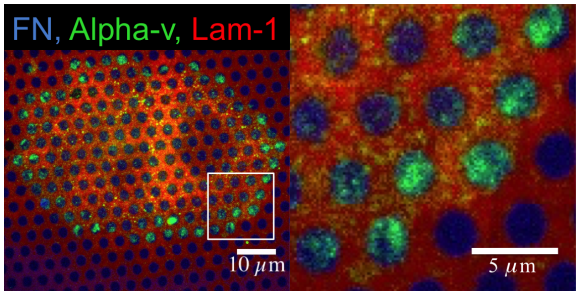

Figure S1: PCs (dif31) placed on a pattern of FN and LM-111 depicted in (Fig. 1 B) with alpha-v integrin labeled (green). Related to Figure 1.

Figure S2

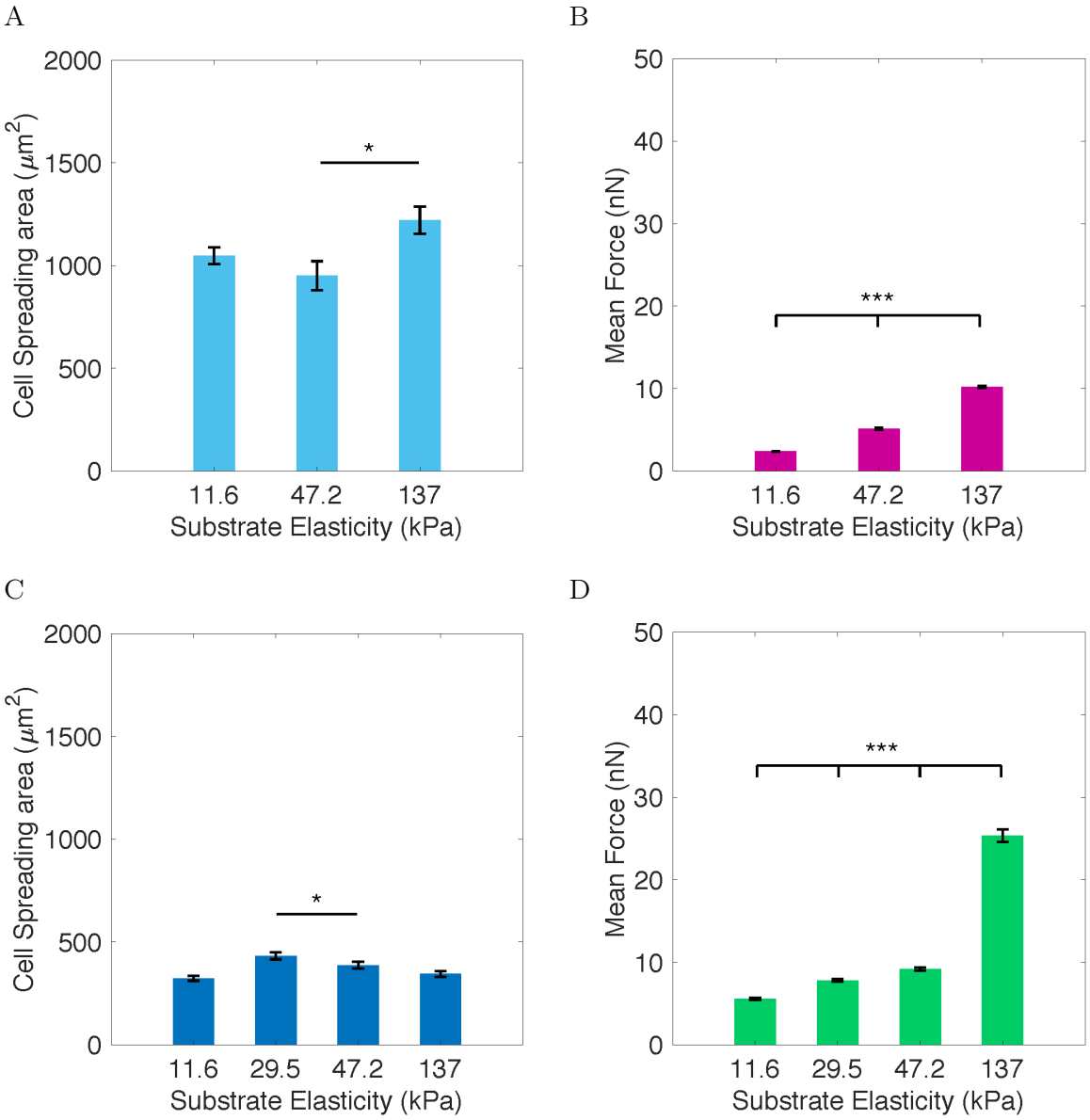

Figure S2: SV80 and 3T3 cells average spreading area and force application. (A) SV80 average cell spreading area on PDMS micropillar arrays after 4 hours incubation. (B) SV80 average force application measured after 4 hours incubation. (C) 3T3 average cell spreading area on PDMS micropillar arrays functionalized with FN after 4 hours incubation. (D) 3T3 average force application measured after 4 hours incubation. All error bars are s.e.m. derived from three independent experiments performed in minimum two replicates. At least 30 cells were analyzed from each sample. NS, $P>0.05$; *$P<0.05$; **$P<0.005$; ***$P<0.0005$ according to Mann - Whitney test. Related to Figure 3.

Figure S3

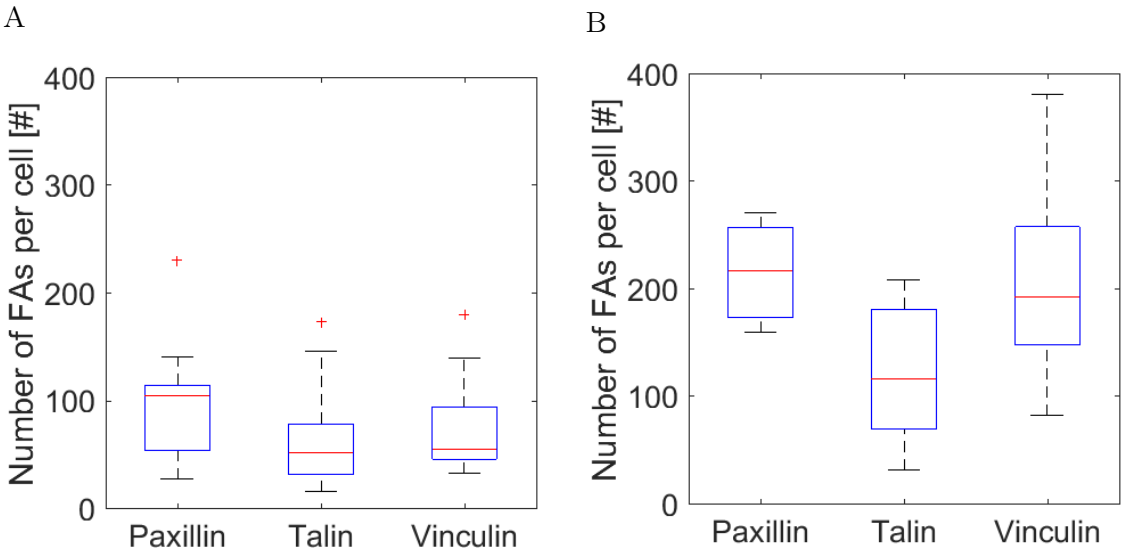

Figure S3: (A) Number of FAs per cell for PCs seeded on 137 kPA micropillar arrays stamped with FN. (B) Number of FAs per cell for PCs seeded on 47,2 kPA micropillar array stamped with FN. Results were obtained after 4 hours incubation from three independent experiments performed in minimum two replicates. At least 30 cells were analyzed from each sample. NS, $P>0.05$; *$P<0.05$; **$P<0.005$; ***$P<0.0005$ according to Mann - Whitney test. Related to Figure 4.

Figure S4

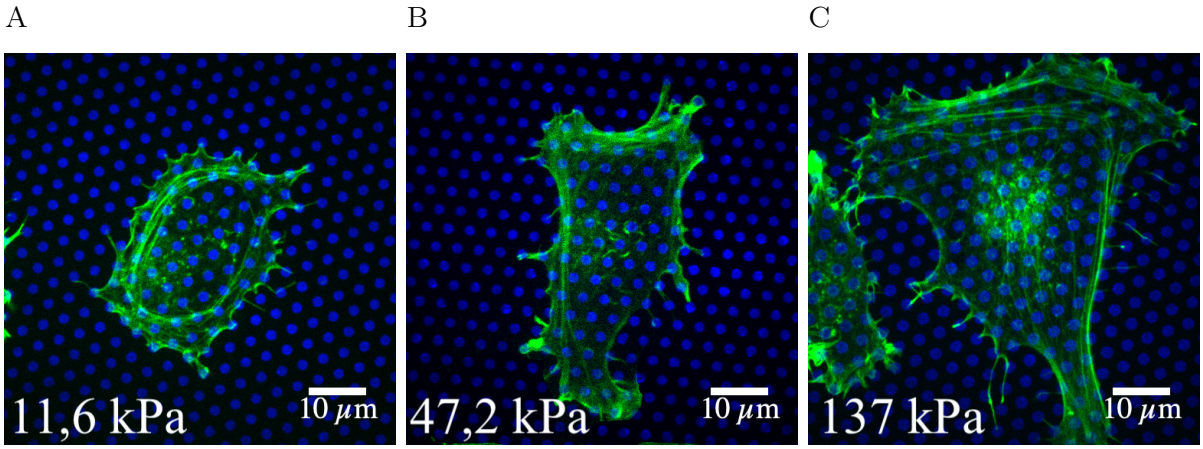

Figure S4: Representative images of the actin cytoskeleton organization of SV80 cells (green) seeded on PDMS micropillar arrays of various stiffness stamped with FN (blue): (A) 11,6 kPa, (B) 47,2 kPa, (C) 137 kPa. Related to Figure 5.